

Article

Influence of Process Parameters on the Mechanical Properties and Corrosion Resistance of Dissimilar Friction Stir Welded Joints of AA2024-O and AA6061-O Aluminum Alloys

Roosvel Soto-Diaz ^{1,*} , Anderson Sandoval-Amador ² , José Escorcia-Gutierrez ³ and Jimy Unfried-Silgado ⁴ ¹ Biomedical Engineering Program, Universidad Simón Bolívar, Barranquilla 080002, Colombia² Department of Engineering, Universidad Loyola Andalucía, 41704 Dos Hermanas, Spain; aasandoval@uloyola.es³ Department of Computational Science and Electronic, Universidad de la Costa, CUC, Barranquilla 080002, Colombia; jescorci56@cuc.edu.co⁴ Research Group ICT, Department of Mechanical Engineering, University of Cordoba, Montería 230002, Colombia; jimyunfried@correo.unicordoba.edu.co

* Correspondence: roosvel.soto@unisimon.edu.co; Tel.: +57-3043622330

Abstract: The influence of the process parameters, traverse, and rotational speeds of dissimilar friction stir welded joints of AA2024-O and AA6061-O aluminum alloys on the corrosion resistance was evaluated. Potentiodynamic tests using a 3.5% NaCl solution, open circuit potential, and polarization curves showed the corrosion behavior for the different welding parameters. These data were correlated with those obtained by mechanical tests (microhardness, tensile, and fracture analysis) and microstructure analysis by optical and scanning electron microscopy. It was observed that the combined effect of the parameters influenced the variation of corrosion resistance. This was evidenced mainly by the improvement of corrosion resistance at 1200 rpm–65 mm·min^{−1}, which was related to the tendency of grain size and heat input presented. The corrosive attacks on the welded joints presented greater affectations in the presence of base material 1 (AA6061-O) with higher metallic dissolution. Corrosion attacks abovementioned were presented in different forms, such as pitting, localized, and selective, and they were observed by scanning electron microscopy. Finally, in corrosive and mechanical terms, the best performing condition was 1200 rpm and 65 mm·min^{−1} compared to the low parameter of 840 rpm and 45 mm·min^{−1}.

Keywords: dissimilar friction welding—agitation; agitated zone; corrosion; potentiodynamic curves



Citation: Soto-Diaz, R.; Sandoval-Amador, A.; Escorcia-Gutierrez, J.; Unfried-Silgado, J. Influence of Process Parameters on the Mechanical Properties and Corrosion Resistance of Dissimilar Friction Stir Welded Joints of AA2024-O and AA6061-O Aluminum Alloys. *Metals* **2024**, *14*, 664. <https://doi.org/10.3390/met14060664>

Academic Editor: Alfonso Paoletti

Received: 11 April 2024

Revised: 16 May 2024

Accepted: 29 May 2024

Published: 3 June 2024



Copyright: © 2024 by the authors. Licensee MDPI, Basel, Switzerland. This article is an open access article distributed under the terms and conditions of the Creative Commons Attribution (CC BY) license (<https://creativecommons.org/licenses/by/4.0/>).

1. Introduction

Friction stir welding was invented and patented by W. Thomas at The Welding Institute (TWI) in England in 1991 [1]. Due to its advantages as a solid-state welding process, FSW has led to the development of important joint applications that have had an impact on the production and use of lightweight alloys [2–4]. This process makes it possible to join metals such as aluminum, magnesium, copper, and steel, including many alloys considered difficult to weld by conventional welding processes [4–6]. Critical factors in fusion welding processes have been related to liquid-solid state changes (including hot cracking and HAZ liquation), melting temperature, cooling rates, phase transformations, and others. These discontinuities could be drastically reduced using FSW, obtaining welded joints with good mechanical properties and acceptable corrosion resistance [7–10]. Key metallurgical factors in FSW aiming to obtain both good mechanical properties and corrosion resistance are grain size refinement and intermetallic precipitate distribution [11–13]. Figure 1 shows the different welding region parameters set in an FSW joint. The FSW regions are the following: base metal A; heat-affected zone B; thermo-mechanically affected zone C; and stirred region, which is the region represented by the letter D. In the stir region occurs

recrystallization phenomena and refinement of grain size, which could lead to very complex behavior in dissimilar welded joints [14–16]. FSW has been successfully used to join several similar aluminum alloys [17–19]. Nevertheless, a wide group of structural components requires joining different materials to take advantage of each one's mechanical, physical, and chemical properties. These joints are called dissimilar welded joints. High-quality dissimilar joints are a true challenge to conventional welding processes [19–24]. The friction stir welding process is a successful alternative in these cases [21,25,26].

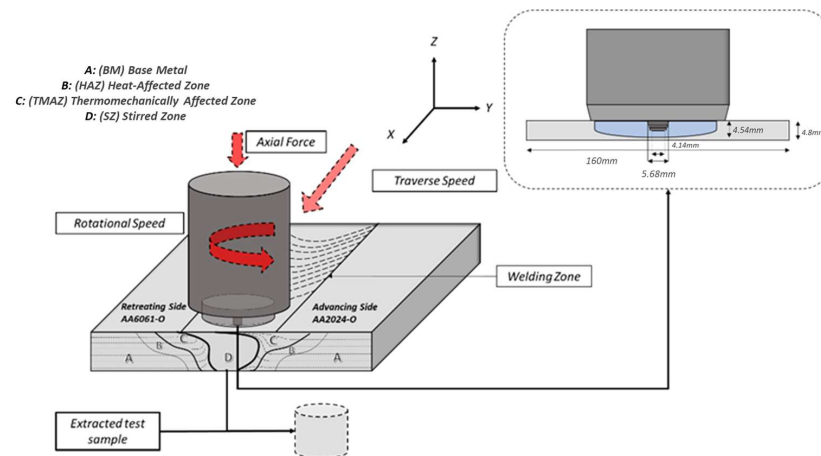


Figure 1. Sketch of FSW process and parameters.

Dissimilar welding joints of AA2xxx and AA6xxx series aluminum alloys have been widely studied, with results mainly focusing on the influence of process parameters on the variation of microstructure and mechanical properties [27–30]. Even though useful process parameter windows have been established, which aim to maximize mechanical properties, there is not much information about the corrosion resistance behavior in this set of welded joints. Paidar et al. [31], investigated the effect of materials positioning on mechanical properties and microstructure of dissimilar friction stir welded AA2024/AA6061 aluminum alloys. They found that positioning is an essential factor that modifies flow patterns, welding regions' hardness, precipitation levels, dislocation density, and maximum tensile strength values. The best behavior was observed when AA2024 was on the advanced side [30]. Kumar et al. [32] and Mohapatra et al. [33] studied the effect of parameters on dissimilar welded joints of AA2024 and AA6082 aluminum alloys. They measured hardness and tensile tests, complemented with metallographic observations. These joints were carried out by varying the welding speed between 30 and 50 mm·min^{−1}, rotational speed between 1200 and 1400 rpm, and the alloy AA2024 placed on the advancing side. They observed a correlation between the mixing pattern and the mechanical properties with process parameters.

The AA6061-O alloy group has primary applications in aircraft and electrical fittings, magnetic parts, brake and hydraulic pistons, appliance fittings, valves, and valve parts. Recently, it has been utilized in energy absorption systems where welding plays a crucial role [34,35]. Conversely, the AA2024 alloy is extensively employed in the aerospace and automotive sectors. Although the annealed version AA2024-O is not directly recommended for use, efforts have been made to explore the advantages of its aging behavior for joining and forming processes [36,37]. Some research has shown satisfactory mechanical and corrosion properties for welded joints in both AA6061-O [38,39] and AA2024-O [40,41] alloys. The dissimilar system of AA6061-O-AA2024-O is utilized in forming processes for aeronautic and automotive components [42]. However, limited studies exist on the welded joints of this dissimilar alloy system. Specific investigations have focused on understanding the relationships between parameters and mechanical behavior in metallic matrix composite materials produced through hard particle addition during welding [43,44]. Due to the potential application of this dissimilar alloy system in complex energy absorption and

refrigeration systems, the significance of studying the corrosion and mechanical properties of their friction stir welded (FSW) joints is growing.

Laska et al. observed in friction stir welded joints of AA6082 alloys that the best corrosion behavior in NaCl 3.5% solution was obtained with the highest revolutionary pitch (between 6.0 and 6.5 rev·mm^{−1}) [45]. Souza et al. studied localized corrosion resistance in friction stir welded joints of AA2198-T8 alloys. They found that in the stir region of these welded joints, the corrosion was intergranular and correlated to T2/TB phases precipitated at intergranular positions [46]. Jandaghi et al. investigated the effects of heat treatment on dissimilar friction stir welded joints of AA2198-AA6013 alloys. These authors observed that thermal conditions promoted massive diffusion and formation of Cu-rich precipitates, mainly on the AA2198 side, which carried out precipitation in grain boundaries and failure in the stir region that contains this alloy [47].

Kumar et al. [32] studied the effect of parameters on the material flow, mechanical properties, and corrosion in dissimilar friction stir welded joints of AA5083–AA6061 alloys. They observed a refined structure in the stir region, which was confined in the onion sub-structure. The mixture of both dissimilar alloys in the stir region was observed at lower traverse and higher rotational speeds. The corrosion resistance of these welded joints increases with decreased traverse speed and increased rotational speed. The width of the onion substructure decreases with increased rotational speed. Both fragmentation and redistribution of intermediate phases were associated with increased rotational speed and corrosion resistance, correlating this with the reduction of sites susceptible to corrosion attack [36]. Finally, Sasikumar et al. [48] evaluated the effects of process parameters on mechanical properties and corrosion resistance on filler-induced friction stir welding of dissimilar AA6082–AA5052 joints. The study's main findings indicated that higher rotational speed improves the mixing of materials in the stirred zone (SZ), decreasing corrosion susceptibility. This is attributed to the more uniform fragmentation and distribution of intermetallic particles, which reduce the formation of potential galvanic cells. It was observed that higher rotational speeds led to better corrosion resistance due to a more homogeneous mixing of materials and a finer and more uniform distribution of intermetallic phases, minimizing sites for galvanic corrosion. Finally, the authors showed that the selection of optimal welding parameters is crucial to maximizing mechanical strength and reducing the corrosion susceptibility of FSW aluminum joints.

Using the data presented in Table 1 and drawing from the examination of characteristic defect types in friction stir welds as outlined in the reference [49], it becomes evident that an optimal parameter range lies between 500 and 1500 rpm and 40 and 200 mm·min^{−1} for dissimilar welded joints of AA6061/AA2024, predominantly employing a taper cylindrical tool (see Figure 2). For this study, values were chosen outside of limits, resulting in a parameter range of 800 to 1200 rpm and 40 to 65 mm·min^{−1}, and using the same tool geometry.

Table 1. Parameters used to obtain FSW joints with AA6061/AA2024.

Base Material	vs (mm·min ^{−1})	w (rpm)	Tool Geometry	Soundness	Reference
AA6061-O	150–400	750–1500	Cylindrical pin	No defects	[38]
	150	1750	Cylindrical threaded	No defects	[50]
AA2024-O	300	300	Conical threaded pin	No defects	[40]
	40	1250	Taper cylindrical	No defects	[51]
AA6061–AA2024	31.5–40	800–2000	Square frustum probe	No defects	[43]
	35–65 *	500–1200	Conical pin	No defects	[52]
	28	710	Taper cylindrical	No defects	[53]
	40	1000	Taper cylindrical	No defects	[54]
	40	500	Conical	No defects	[55]
	40	900–1400	Conical	No defects	[56]

* Evaluating the entire interval.

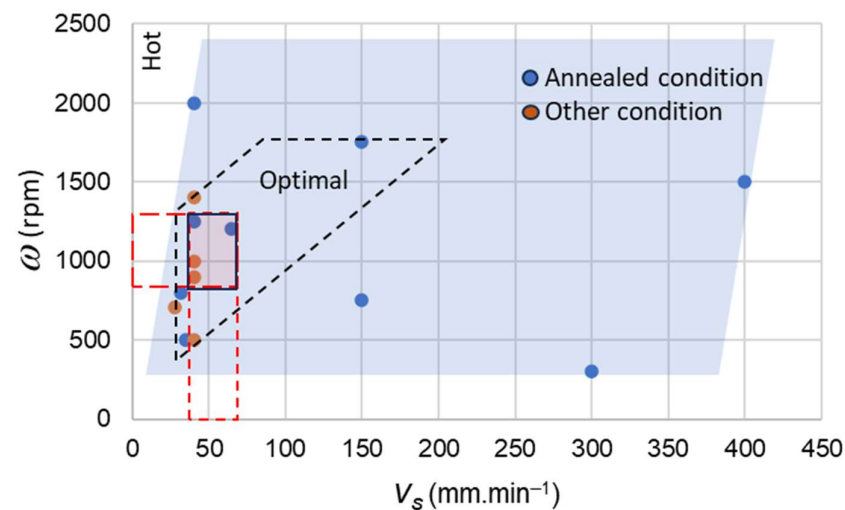


Figure 2. Graphical analysis of parameters used in FSW the system AA6061/AA2024.

Due to scarce research evidence, the goal of this work is to evaluate the influence of process parameters, traverse, and rotational speeds on the corrosion resistance behavior, mechanical properties, and thermal cycling of dissimilar solder joints.

2. Materials and Methods

2.1. Materials

In this work, plates of AA2024-O and AA6061-O aluminum alloys were used with dimensions $80 \times 150 \times 4.8$ mm. Table 2 shows the chemical composition of these aluminum alloys obtained by mass spectrometry.

Table 2. Chemical composition of materials [38].

Chemical Composition (wt.%)							
Material	Al	Si	Fe	Cu	Mn	Mg	Others
AA2024-O	Bal.	0.099	0.095	4.672	0.445	1.627	0.011
AA6061-O	Bal.	0.561	0.366	0.187	0.067	0.848	0.241

2.2. Welded Joints

A butt-welding joint configuration was used with the AA2024-O plates located on the advancing side (AS) and the AA6061-O plates on the retreating side (RS). The welding process was carried out in an FSW machine TTI model RM1 (Transformation brand Technologies Inc.® Elkhart, IN, USA), as shown in Figure 3a. The tool used to develop the welded joints was fabricated of H13 steel with a concave shoulder and a threaded conical pin, as shown in Figure 3b,c. An experimental design 2k with two factors named: traverse speed and rotation speed, and each one with two levels (high and low) was developed, as shown in Table 3. HH represents the codified levels for the combination of high values and LL for the low values. Peak temperatures were measured by recording the temperature as a function of elapsed time using a type K thermocouple arranged in the tool shoulder.

Table 3. Tool dimensions and process parameters.

Identification Welding Samples	Traverse Speed (mm.min ⁻¹)	Rotational Speed (rpm)	Pin Shape	Shoulder Diameter Ø (mm)	Pin Length (mm)	Tool Tilt Angle (°)
HH	65	1200	Truncated cone	22	4.54	2
LL	45	840				

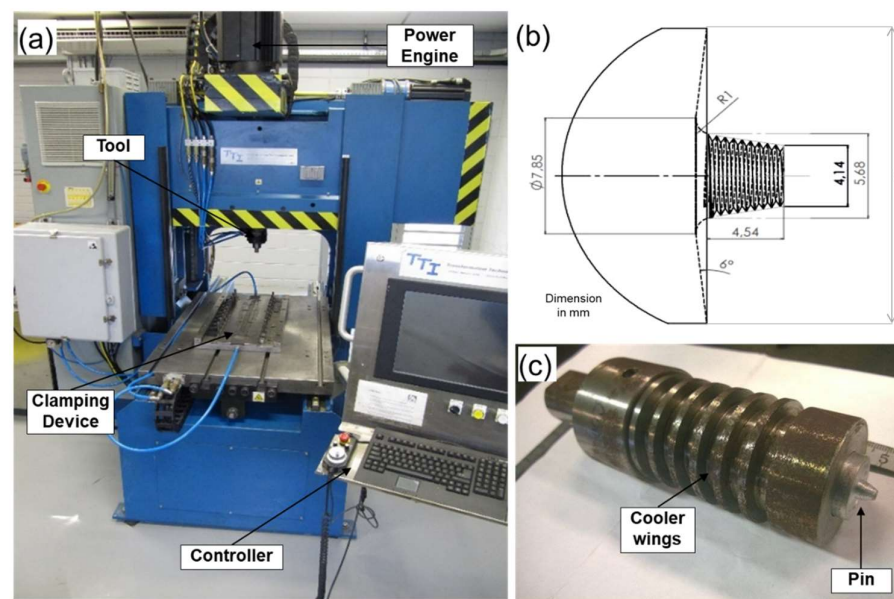


Figure 3. (a) FSW machine Transformation brand Technologies Inc.[®] (TTI) model RM1, (b) Geometry of the shoulder and tool pin and (c) tool for welding.

2.3. Experimental Sample Extraction

Figure 4a shows the location of the different samples for testing. Figure 4b shows the samples for tensile tests, which are based on ASTM-E8(/E8M-22) [57] standard. Figure 4d shows the sample extracted for metallographic analysis under the ASTM E3-11 [58] standard and the location of the sequence of the microhardness measurements developed by ASTM-E384-17 [59]. Figure 4c shows the corrosion samples extracted from the welded joint center corresponding to the stirred region, which occurs in the mixture of the base materials; for the identification of specimens, the codification was used, as shown in Table 3. All samples were obtained using a water jet cut, aiming not to introduce alterations in the welded microstructure.

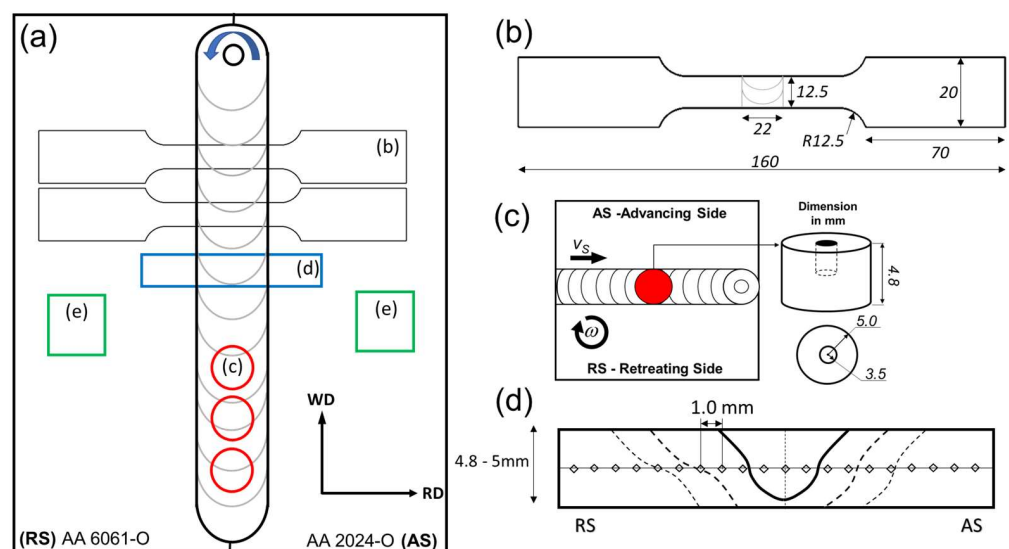


Figure 4. Experimental samples. (a) Location of samples in a welded joint. (b) Tensile test specimen. (c) Corrosion test specimen. (d) Microstructure and hardness sample (e) X-ray specimens.

2.4. Macro and Microstructural Analysis

Aiming to prepare both samples for macroscopic and microscopic analysis and to evaluate the material's structure, a cut was made perpendicular to the weld. Once cut, the

samples were prepared based on ASTM 3-11 standard [58], cleaned, ground, polished, and etched with modified Poulton's reagent (25 mL Poulton + 12.5 mL HNO₃ + 20 mL solution of 3 g of H₂CrO₄ per 10 mL H₂O). Microstructure of the weldments and base metals, fracture analysis, and the surface morphologies of the corroded specimens were examined using optical microscopy (OM) with an Olympus[®] EX51 (Tokyo, Japan) and scanning electron microscopy (SEM) using a JEOL[®] JSM-7100F FEG (Tokyo, Japan), respectively.

2.5. X-ray Diffraction

X-ray diffraction tests were developed in a PANalytical X'Pert PRO MRD XL. The specimens used were 20 × 20 × 4.8 mm and were extracted, as shown in Figure 4e. Specimens were ground to 800 sandpapers before XRD measurements. The radiation used in the test was Cu K α type ($L = 1.5405 \text{ \AA}$) operating at 45 kV and 40 mA. Analysis was carried out in an angle range from 20° to 110° with a 0.02° pass.

2.6. Hardness Measurements

Vickers microhardness test was developed using a Zwick-Roell[®] HZHVuM micro-durometer (Ulm, Germany) and a load of 100 gf for 10 s. The microhardness measurement profiles were made in the middle zone crossing welding regions, as shown in Figure 4d. There were 37 indentations at 1 mm between each one, starting from the center of the weld toward the advancing and reversing sides, respectively.

2.7. Tensile Test

A tensile test was performed on samples for each welded joint in triplicate. These tests were carried out in a universal test machine Shimadzu AG-X of 100 kN using a displacement speed of 5 mm·min^{−1}. All tensile tests were performed perpendicular to the welding direction and at room temperature.

2.8. Corrosion Tests

The corrosion test was carried out by assembly of an electrochemical cell coupled to a Solartron[®] Analytical console (Bognor-Regis, UK). The exposed area of the samples used as working electrodes was 78.5 mm², a saturated calomel electrode was used as a reference electrode, and a graphite high-purity rod was used as the counter electrode. NaCl saline solution at 3.5% *w/v* was used, aiming to simulate the chloride effects on welding regions. The polarization curves were carried out using 1 mV·s^{−1} as the scan rate, within a potential range between −0.25 V and 1.0 V concerning the open circuit potential. The corrosion potentials, the corrosion current, and the corrosion rates of the samples were determined from de Tafel curves based on the ASTM G5-A and ASTM G69-20 [60,61]. All measurements were performed in triplicate, and average values were reported.

3. Results and Discussion

3.1. Microstructure and Welding Results

Figure 5 shows the results of the microstructure characterization of the as-received state AA6061-O aluminum alloy. Optical and scanning electron microscopy images (Figure 5a,b) show that this alloy presents elongated grains of Al-rich γ phase and irregular size rounded particles are heterogeneously dispersed, probably of β -Mg₂Si (Figure 5c), as evidenced by XRD results and previous works [50,62,63].

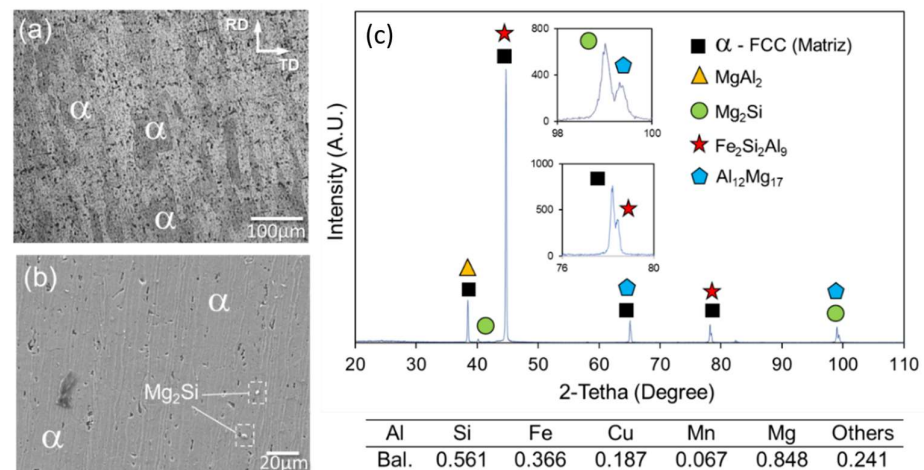


Figure 5. Characterization of AA6061-O as-received metal base. (a) Optical and (b) SEM images of microstructure. (c) X-ray diffraction results and XRD patterns obtained at the interface.

Figure 6 shows the results of the microstructure characterization of the as-received state AA2024-O aluminum alloy. The microstructure of this alloy shows elongated grains of Al-rich γ phase with small precipitates (probably of Al_2Cu) decorating the grain boundaries and heterogeneously distributed and rounded precipitates (probably of Al_2CuMg), which were observed through electron microscopy and DRX, which was reported by other works [37,64,65].

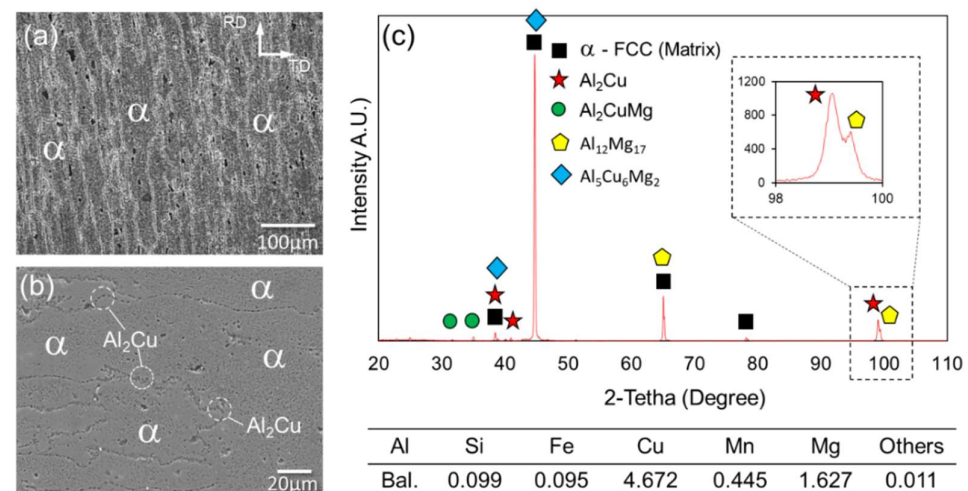


Figure 6. Characterization of AA2024-O as-received metal base. (a) Optical and (b) SEM images of microstructure. (c) X-ray diffraction results and XRD patterns obtained at the interface.

Figure 7 shows the appearance of welding beads obtained with HH and LL parameters (see Table 3). Figure 7a shows a welded joint obtained with HH parameters, displaying a moderate burr and rough texture. A similar aspect was observed in the welded joint obtained with LL parameters, although with a smoother surface (Figure 7b). Both welded joints presented favorable acceptance criteria because no serious visual discontinuities existed.

Figures 8 and 9 show the cross-sections of welded joints obtained using the HH and LL set of parameters, respectively. The microstructural characterization shows differences in the flow pattern produced in the stir region due to the process parameters used. In the HH conditions, the stir zone is wider than the LL conditions, as shown in Figure 8. Moreover, there was a tendency to form ribbon flash, nugget collapse, flow arm shoulder, and discontinuities called transpositions because high advance speed prevented homoge-

nization in the upper zone of the nugget [49,66,67]. In LL, a stir region with a narrow shape of a wine glass was observed exhibiting a limited mixture of both base materials. In this welded joint, characteristics such as laminar interleaving, whipping flow patterns, forging zones, and formation of an interlaminar at the stir zone were noticed, which is shown in Figure 9 [49]. Welding regions correspond to SZ: stirred zone, HAZ: heat-affected zone, TMAZ: thermomechanical-affected zone, and BM: base metal.

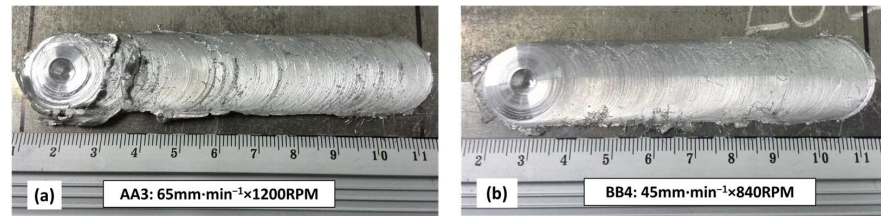


Figure 7. Macroscopic characteristics of welded joints using the set combination: (a) HH parameters and (b) LL parameters.

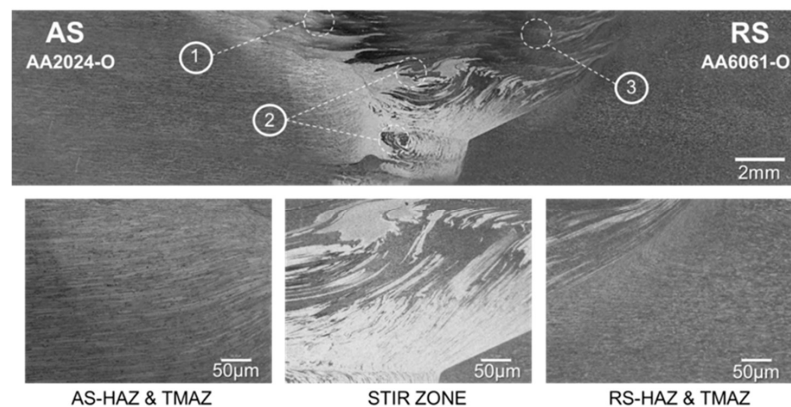


Figure 8. Cross-section microstructure of welded joint obtained with HH parameters. (1) Ribbon flash, (2) nugget collapse, (3) flow arm shoulder.

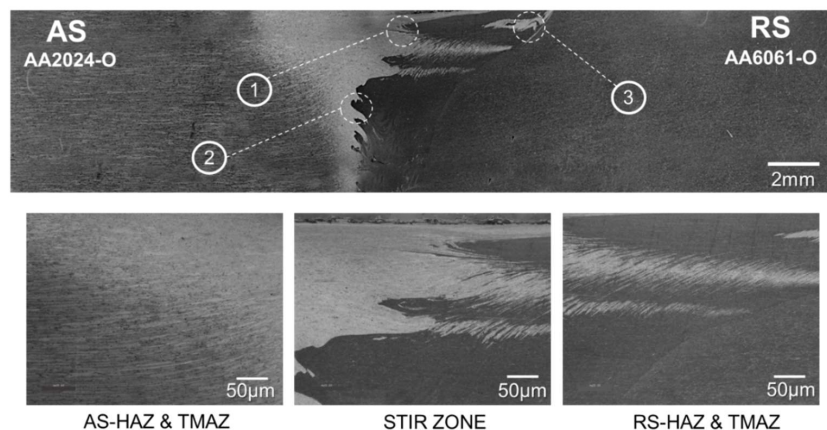


Figure 9. Cross-section microstructure of welded joint obtained with LL parameters. (1) Laminar interleaving, (2) whipping flow patterns, (3) forging zones.

3.2. Thermal and Process Parameters Analysis

Table 4 summarizes the spindle torque results and peak temperatures experimentally measured during welding. Heat input (HI) was also calculated using Equation (1).

$$HI = \frac{2\pi\omega\tau}{1000v} \left[\text{kJ} \cdot \text{mm}^{-1} \right] \quad (1)$$

Table 4. Spindle torque, heat input, and peak temperatures were measured experimentally.

Condition	Rotational Speed (rpm)	Traverse Speed (mm·min ^{−1})	ω/v Ratio	Peak of Temperature (°C)		Torque (N·m)	Heat Input (kJ·mm ^{−1})
				Adv.	Ret.		
HH	1200	65	18.5	313	272.2	46	5.33
LL	840	45	18.7	464.3	309	53.5	6.27

In Equation (1), ω is rotational speed, τ is spindle torque, and v is advance speed [7].

In friction stir welding, the ratio of rotational to traverse speed (ω/v) is a very important parameter aiming to establish valuable relationships among thermal history, process parameters, and properties of welded joints. When the ω/v ratio is increased, the input is increased, the tendency of grain growth is intensified, the density of dislocations is decreased, and hardness is decreased [68]. In the case of the truncated conical and threaded pin used in this investigation, the ratio ω/v to generate defect-free welded joints is recommended to use a value of 2.0 or larger [68,69]. By Table 3, welding conditions HH and LL reached a similar ratio value (ω/v). However, calculated heat input and allowed maximum peak temperature in the welded joint are approximately 15% and 50% each different, respectively. Then, it is expected that welded joints with HH conditions present a tendency to refine grain size in the stirred zone and higher hardness values than in LL conditions.

3.3. Microhardness and Tensile Test Results

Profiles of microhardness measurement results are shown in Figure 10a. In general, for evaluated conditions, the behavior of microhardness profiles shows an increase in the welded joint regions due to the annealed condition of base metals and solid-state deformation effects produced by the FSW process. Base metals displayed average microhardness values of 42 HV for AA6061-O and 56 HV for AA2024-O, which are coherent with other works [37,50,63]. The highest value of microhardness (131 HV) was obtained in the welded joints with HH conditions, and it was located near to the TMAZ of the advancing side (2024-O). This increased hardness could be due to the tendency of grain size refinement expected in the stir zone, a larger mixture homogenization observed, and the flow pattern in the nugget region of HH conditions. Welded joints obtained using LL conditions exhibited a maximum hardness value (103 HV), which is a lower value than obtained with HH conditions. A possible explanation for the behavior above could be narrow-wide, the lowest mixture homogenization, and the tendency of grain size growth in the stir zone due to the peak of temperature allowed there [70–72].

Figure 10b and Table 5 show the summarized results of the tensile test carried out on welded joints and base metals. Results showed that welded joints fabricated with HH and LL parameters disclosed statistically similar values of tensile properties, and both are less than base metals. Base metal AA-6061-O displayed an ultimate strength of 124 MPa, yield strength of 62.1 MPa, and an elongation percentage of 25%. On the other hand, base metal AA-2024-O allowed an ultimate strength of 86 MPa, yield stress of 86.6 MPa, and an elongation percentage of 20%. An evident reduction of yield strength in both welded conditions concerning the base metals and similar behavior regarding ultimate strength and elongation percentage more like base metal AA-6061-O values were observed. All fracture regions were located at the AA-6061-O side. For the HH conditions, the microstructure homogenization of both materials in the stir region probably increased the quantity of AA2024-O in the mixture, lightly increasing the tensile properties of a welded joint compared to LL conditions [41,43]. The probable largest density of dislocations produced by the lightly high ratio (ω/v) of LL conditions compared to HH conditions could explain the apparent higher yield strength observed in this welded joint [37].

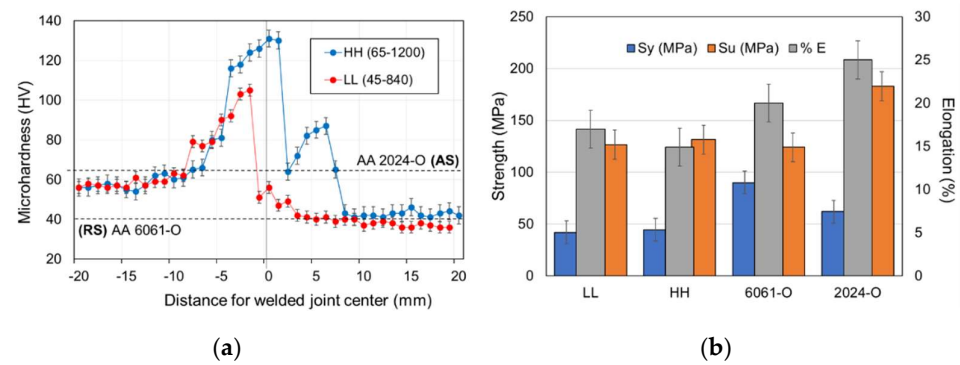


Figure 10. (a) Microhardness cross-section profiles and (b) tensile properties in function of process parameters and base metals. Sy: yield strength, Su: ultimate strength, and %E: percentage elongation.

Table 5. Summary of results of experimental and calculated welding parameters.

Welding Conditions	Tensile Strength S_u (MPa)	Yield Strength S_y (MPa)	Elongation e (%)	Tendency of Grain Size
AA6061-O	124.0 ± 6.2	62.0 ± 3.1	25.0 ± 1.3	Coarsening
AA2024-O	183.0 ± 9.2	89.6 ± 4.5	20.0 ± 1.0	Coarsening
HH (65–1200)	126.6 ± 6.3	44.5 ± 2.2	14.9 ± 0.7	Refinement
LL (45–840)	131.4 ± 6.6	42.0 ± 2.1	17.0 ± 0.9	Average

Figure 11 shows the scanning electron microscopy images of fractured surfaces of the welded joints. Images exhibited slight differences in fracture mechanism for each evaluated welding condition. In the HH welded conditions (Figure 11a,b), a ductile fracture mechanism was observed displaying elongated and deformed dimples. On the other hand, in the LL welded condition (Figure 11c,d), the combined mechanism between faceted and dimple fractures with less severe plastic deformation than the HH conditions (yellow arrows) was observed. The difference between fracture mechanisms observed is possibly due to the difference in mixing pattern for both welding conditions and a complex interaction with precipitate movement during the welding process [31].

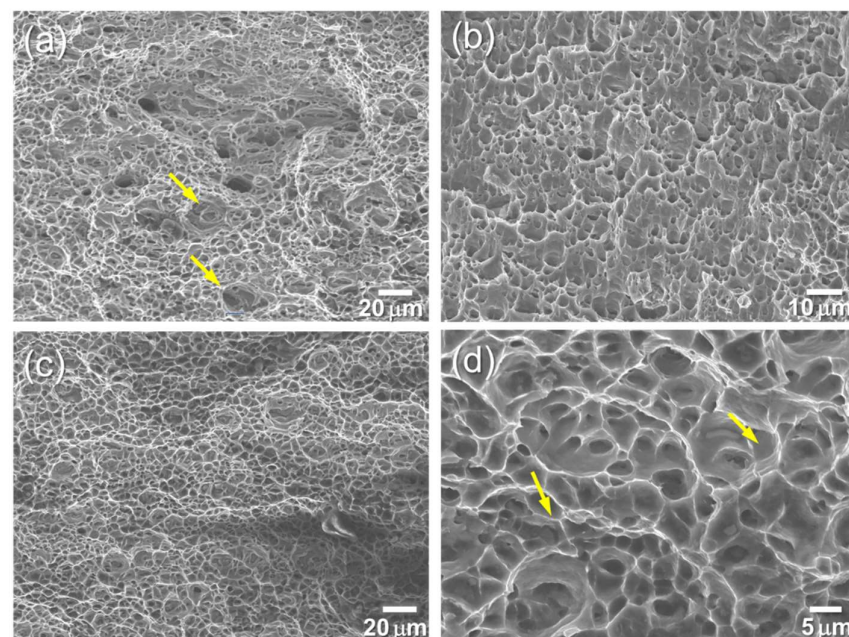


Figure 11. (a,b) SEM micrographs at the fracture surface of HH, (c,d) SEM micrographs at the fracture surface of LL.

3.4. Corrosion Results Analysis

Figure 12 shows the electrochemical behavior obtained with base metals and welded joints immersed in 3.5% *w/v* NaCl solution (pH = 6.0). Changes in the open circuit potential (OCP) (Figure 12a) of the aluminum alloys start from an increasingly negative initial OCP during the first 10 min and last until stabilized at a rest potential. The potential shift to a more anodic direction is often associated with the samples' chemical composition and the formation of a protective passive film at the surface. The curves' OCP obtained from welded joints exhibited a relatively stable steady OCP around -720 mV, close to the critical pitting potential values of AA6061 and AA2024 [72–74]. This behavior is evidence of mixture homogenization and heat plasticity in the stir region. Figure 12b shows typical potentiodynamic curves obtained with samples of AA6061 and AA2024 aluminum alloy exposed to 3.5% *w/v* NaCl solution (pH = 6.0). The curves of HH and LL welding joint conditions show similar behavior compared with base materials. It was observed that all studied samples exhibit a low cathodic current density, and these cathodic current density values are equivalent to corrosion rates. Moreover, the anodic reaction on all curves appears to be controlled by the pitting of the surfaces; it is associated with a rapid increase in current, which can be observed in the anodic slopes with values close to zero. The results of the Tafel analyses are summarized in Table 6. AA6061-O alloy displayed a corrosion potential of -741 mV compared to -659 mV of AA2024-O alloy [74,75]. The welded joint with HH conditions presented a similar behavior to AA6061-O alloy; it was due to Mg content, which generates a passivating effect, enhanced by the tendency to refinement of grain size in the stir region [72], obtaining a low corrosion rate. Welded joints with LL conditions presented a behavior like the AA2024-O alloy, which was related to mixture heterogeneity obtained during the welding process [31,33].

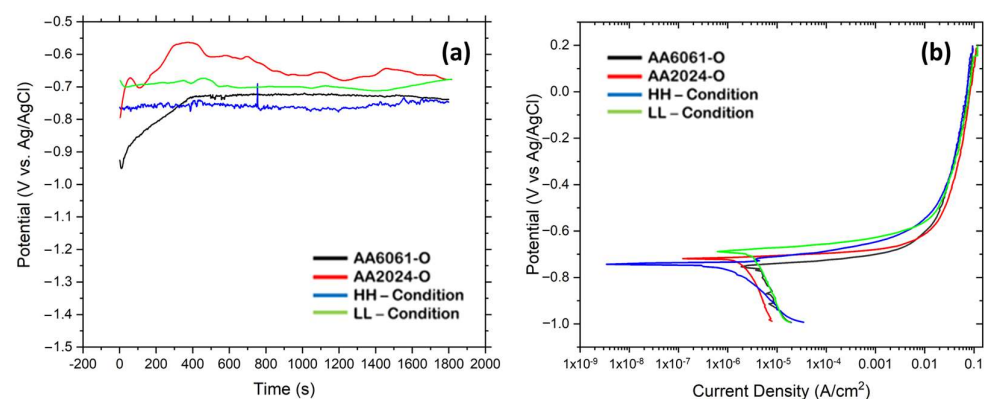


Figure 12. (a) Open circuit potential and (b) potentiodynamic polarization curves experimentally measured.

Table 6. Electrochemical parameters were obtained from the potentiodynamic polarization curves.

Sample	E_{corr} (mV)	I_{corr} ($\text{A} \cdot \text{cm}^{-2}$)	Corr. Rate (mm per Year)
AA6061-O	-741	2.07×10^{-6}	1.39×10^{-1}
AA2024-O	-659	4.95×10^{-6}	6.39×10^{-2}
HH	-729	8.04×10^{-7}	3.01×10^{-2}
LL	-713	3.28×10^{-6}	7.69×10^{-2}

Images obtained by scanning electron microscopy of the appearance of the surface in the stir region after corrosion tests are shown in Figure 13. Images in Figure 13a,b show the effects of corrosion in base metals AA6061-O and AA2024-O, respectively. In AA 6061-O alloy, generalized corrosion is observed in a high percentage of the analyzed surface, and multiple areas are observed where a localized attack of the electrolyte is evident. Similar

behavior is observed on the analyzed surface of the AA 2024-O alloy; however, the areas of generalized and localized corrosion are present in a smaller proportion.

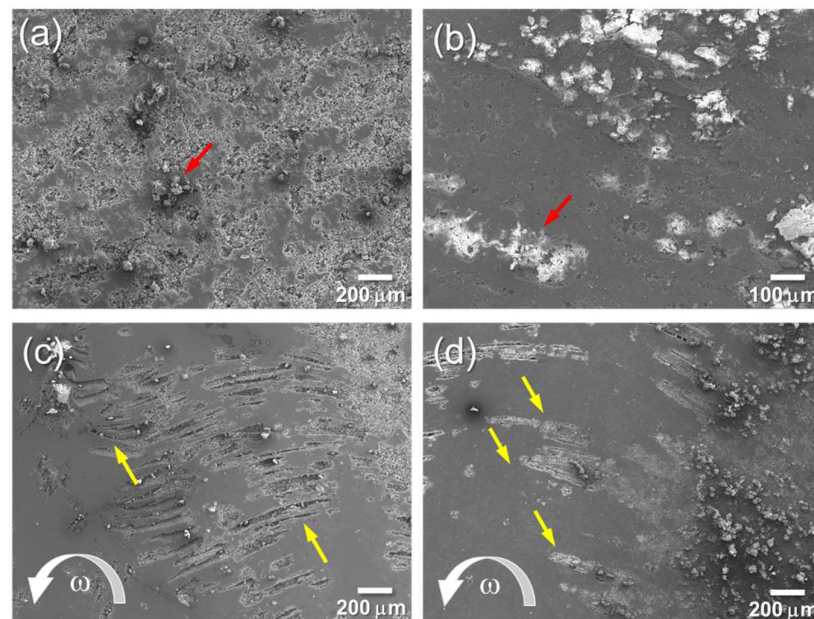


Figure 13. SEM images of the surface of dissimilar joints (a) AA6061-O, (b) AA2024-O, welded joints with (c) HH conditions, and (d) LL conditions.

Figure 13c,d displays the effects of corrosive attacks in welded joints with HH and LL conditions, respectively. This last set of images showed a series of flow patterns (yellow arrows) produced by the stirring effect during the welding process at the stir region. Localized attacks were observed in both welded joints, mainly where the AA6061-O alloy is present due to its low corrosion resistance (yellow arrows). The areas with the least affection are attributed to the presence of the AA2024-O alloy. Likewise, selective attacks were observed with the same orientation of the rotational movement in the agitation region produced by the tool. It was observed that in the HH conditions, the corroded areas are more abundant but narrower and thinner than in the LL conditions. As mentioned above, these characteristics are probably produced by a greater homogenization and refinement of the grain in the HH conditions, which is consistent with the corrosion rate behavior.

4. Conclusions

The following conclusions are summarized from the analyzed results:

1. The increasing rotational speed influenced the flow pattern at the stir region, producing a tendency to refinement of grain and a higher homogeneous mixture between base metals, which affected corrosion and mechanical properties.
2. Peak temperature, torque, and heat input were correlated to rotational speed, and the plasticizer heats more than the (ω/v) ratio. Evaluated experimental welding conditions in this work showed that HH conditions (1200 rpm) and LL conditions (640 rpm) displayed similar (ω/v) ratio values. Still, the first set displayed a wider and homogeneous mixture stir region.
3. The hardness measurements in the stir region were higher for HH conditions (1200 rpm) because of the tendency to grain refinement and higher mixture between base metals. Little differences in (ω/v) ratio values could explain the scarce differences between tensile properties of HH and LL conditions via increasing.
4. The corrosion behavior of AA6061-O/AA2024-O FSW dissimilar welded joints was highly influenced by pattern flow, i.e., by homogenization of the mixture and the tendency to refinement of grain in the stir region. The higher rotational speed displayed

a more homogenized mixture and tendency to grain refinement, producing narrower and finer corroded regions in the stir region due to the high dissolution area's effect associated with the presence of AA6061-O.

Author Contributions: Conceptualization, R.S.-D. and J.U.-S.; Methodology, A.S.-A., J.E.-G. and J.U.-S.; Formal analysis, R.S.-D., A.S.-A., J.E.-G. and J.U.-S.; Investigation, R.S.-D., J.E.-G. and J.U.-S.; Resources, J.E.-G. and J.U.-S.; Writing—original draft, R.S.-D., A.S.-A. and J.U.-S.; Writing—review and editing, R.S.-D., A.S.-A., J.E.-G. and J.U.-S.; Visualization, J.U.-S.; Supervision, J.U.-S.; Project administration, J.U.-S.; Funding acquisition, J.U.-S. All authors have read and agreed to the published version of the manuscript.

Funding: The authors are grateful to Universidad Autónoma del Caribe for their financial support for this research through project CONV-I-004-P012.

Data Availability Statement: The raw data supporting the conclusions of this article will be made available by the authors on request.

Acknowledgments: The authors wish to acknowledge the Brazilian Center for Research in Energy and Materials (CNPEM) and Instituto Tecnológico Metropolitano (ITM). The authors are grateful to Universidad Autónoma del Caribe and Universidad Simón Bolívar for financial support.

Conflicts of Interest: The authors declare that they have no conflicts of interest. The funders had no role in the design of the study; in the collection, analyses, or interpretation of data; in the writing of the manuscript, or in the decision to publish the results.

References

1. Thomas, W.M.; Nicholas, E.D.; Needham, J.C.; Murch, M.G.; Temple-Smith, P.; Dawes, C.J. Friction Stir Butt Welding. U.S. International Patent No. PCT/GB92/02203, 6 December 1991.
2. Bhardwaj, N.; Narayanan, R.G.; Dixit, U.; Hashmi, M. Recent developments in friction stir welding and resulting industrial practices. *Adv. Mater. Process. Technol.* **2019**, *5*, 461–496. [\[CrossRef\]](#)
3. Soori, M.; Asmael, M.; Solyali, D. Recent development in friction stir welding process: A review. *SAE Int. J. Mater. Manuf.* **2020**, *14*, 63–80. [\[CrossRef\]](#) [\[PubMed\]](#)
4. Isa, M.S.M.; Moghadasi, K.; Ariffin, M.A.; Raja, S.; bin Muhamad, M.R.; Yusof, F.; Jamaludin, M.F.; bin Yusoff, N.; bin Ab Karim, M.S. Recent research progress in friction stir welding of aluminium and copper dissimilar joint: A review. *J. Mater. Res. Technol.* **2021**, *15*, 2735–2780. [\[CrossRef\]](#)
5. Rudrapati, R. Recent advances in joining of aluminum alloys by using friction stir welding. In *Mass Production Processes*; IntechOpen: London, UK, 2019.
6. Chen, G.; Zhang, S.; Zhu, Y.; Yang, C.; Shi, Q. Thermo-mechanical analysis of friction stir welding: A review on recent advances. *Acta Met. Sin.* **2020**, *33*, 3–12. [\[CrossRef\]](#)
7. Soto-Díaz, R.; Sandoval-Amador, A.; Unfried-Silgado, J. Experimental evaluation of rotational and traverse speeds effects on corrosion behavior of friction stir welded joints of aluminum alloy AA5052-H32. *Int. J. Adv. Manuf. Technol.* **2021**, *115*, 3213–3223. [\[CrossRef\]](#)
8. Du, C.; Pan, Q.; Chen, S.; Tian, S. Effect of rolling on the microstructure and mechanical properties of 6061-T6 DS-FSW plate. *Mater. Sci. Eng. A* **2020**, *772*, 138692. [\[CrossRef\]](#)
9. Moreto, J.; dos Santos, M.; Ferreira, M.; Carvalho, G.; Gelamo, R.; Aoki, I.; Taryba, M.; Filho, W.B.; Fernandes, J. Corrosion and corrosion-fatigue synergism on the base metal and nugget zone of the 2524-T3 Al alloy joined by FSW process. *Corros. Sci.* **2021**, *182*, 109253. [\[CrossRef\]](#)
10. Montes-González, F.A.; Rodríguez-Rosales, N.A.; Ortiz-Cuellar, J.C.; Muñoz-Valdez, C.R.; Gómez-Casas, J.; Galindo-Valdés, J.S.; Gómez-Casas, O. Experimental Analysis and Mathematical Model of FSW Parameter Effects on the Corrosion Rate of Al 6061-T6-Cu C11000 Joints. *Crystals* **2021**, *11*, 294. [\[CrossRef\]](#)
11. Patel, V.; Li, W.; Vairis, A.; Badheka, V. Recent development in friction stir processing as a solid-state grain refinement technique: Microstructural evolution and property enhancement. *Crit. Rev. Solid State Mater. Sci.* **2019**, *44*, 378–426. [\[CrossRef\]](#)
12. Wang, P.-J.; Ma, L.-W.; Cheng, X.-Q.; Li, X.-G. Influence of grain refinement on the corrosion behavior of metallic materials: A review. *Int. J. Miner. Met. Mater.* **2021**, *28*, 1112–1126. [\[CrossRef\]](#)
13. Sivaraj, P.; Hariprasath, P.; Rajarajan, C.; Balasubramanian, V. Analysis of grain refining and subsequent coarsening along on adjacent zone of friction stir welded armour grade aluminium alloy joints. *Mater. Res. Express* **2019**, *6*, 066566. [\[CrossRef\]](#)
14. Cai, W.; Daehn, G.; Vivek, A.; Li, J.; Khan, H.; Mishra, R.S.; Komarasamy, M. A state-of-the-art review on solid-state metal joining. *J. Manuf. Sci. Eng.* **2019**, *141*, 031012. [\[CrossRef\]](#)

15. Heidarzadeh, A.; Mironov, S.; Kaibyshev, R.; Çam, G.; Simar, A.; Gerlich, A.; Khodabakhshi, F.; Mostafaei, A.; Field, D.; Robson, J.; et al. Friction stir welding/processing of metals and alloys: A comprehensive review on microstructural evolution. *Prog. Mater. Sci.* **2021**, *117*, 100752. [\[CrossRef\]](#)
16. Ahmed, M.M.Z.; Ataya, S.; Seleman, M.M.E.S.; Allam, T.; Alsaleh, N.A.; Ahmed, E. Grain structure, crystallographic texture, and hardening behavior of dissimilar friction stir welded aa5083-o and aa5754-h14. *Metals* **2021**, *11*, 181. [\[CrossRef\]](#)
17. Jacquin, D.; Guillemot, G. A review of microstructural changes occurring during FSW in aluminium alloys and their modelling. *J. Am. Acad. Dermatol.* **2021**, *288*, 116706. [\[CrossRef\]](#)
18. Janeczek, A.; Tomków, J.; Fydrych, D. The influence of tool shape and process parameters on the mechanical properties of AW-3004 aluminium alloy friction stir welded joints. *Materials* **2021**, *14*, 3244. [\[CrossRef\]](#) [\[PubMed\]](#)
19. Vimalraj, C.; Kah, P. Experimental review on friction stir welding of aluminium alloys with nanoparticles. *Metals* **2021**, *11*, 390. [\[CrossRef\]](#)
20. Xue, X.; Wu, X.; Liao, J. Hot-cracking susceptibility and shear fracture behavior of dissimilar Ti6Al4V/AA6060 alloys in pulsed Nd: YAG laser welding. *Chin. J. Aeronaut.* **2021**, *34*, 375–386. [\[CrossRef\]](#)
21. Sun, Y.; Gong, W.; Feng, J.; Lu, G.; Zhu, R.; Li, Y. A Review of the Friction Stir Welding of Dissimilar Materials between Aluminum Alloys and Copper. *Metals* **2022**, *12*, 675. [\[CrossRef\]](#)
22. Adamus, K.; Lacki, P. Assessment of Aluminum FSW Joints Using Ultrasonic Testing. *Arch. Met. Mater.* **2017**, *62*, 2399–2404. [\[CrossRef\]](#)
23. Lacki, P.; Derlatka, A. Experimental and numerical investigation of aluminium lap joints made by RFSSW. *Meccanica* **2016**, *51*, 455–462. [\[CrossRef\]](#)
24. Lacki, P.; Derlatka, A.; Więckowski, W.; Adamus, J. Development of FSW Process Parameters for Lap Joints Made of Thin 7075 Aluminum Alloy Sheets. *Materials* **2024**, *17*, 672. [\[CrossRef\]](#) [\[PubMed\]](#)
25. Bhushan, R.K.; Sharma, D. Green welding for various similar and dissimilar metals and alloys: Present status and future possibilities. *Adv. Compos. Hybrid Mater.* **2019**, *2*, 389–406. [\[CrossRef\]](#)
26. ShivaKumar, G.N.; Rajamurugan, G. Friction stir welding of dissimilar alloy combinations—A Review. *Proc. Inst. Mech. Eng. Part C J. Mech. Eng. Sci.* **2022**, *236*, 6688–6705. [\[CrossRef\]](#)
27. Battina, N.M.R.; Vanthala, V.S.P.; Chirala, H.K. Effect of friction stir welding process parameters on mechanical and metallurgical behavior of AA6061-T6 and AA2017-T6 tailored blanks. *Eng. Res. Express* **2021**, *3*, 025043. [\[CrossRef\]](#)
28. Al-Sabur, R. Tensile strength prediction of aluminium alloys welded by FSW using response surface methodology—Comparative review. *Mater. Today Proc.* **2021**, *45*, 4504–4510. [\[CrossRef\]](#)
29. Sindhuja, M.; Neelakrishnan, S.; Davidson, B.S. Effect of Welding Parameters on Mechanical Properties of Friction Stir Welding of Dissimilar Metals—A Review. *IOP Conf. Series Mater. Sci. Eng.* **2021**, *1185*, 012019. [\[CrossRef\]](#)
30. Verma, S.; Misra, J.P. Experimental investigation on friction stir welding of dissimilar aluminium alloys. *Proc. Inst. Mech. Eng. Part E J. Process. Mech. Eng.* **2021**, *235*, 1545–1554. [\[CrossRef\]](#)
31. Paidar, M.; Vignesh, R.V.; Khorram, A.; Ojo, O.O.; Rasoulpouraghdam, A.; Pustokhina, I. Dissimilar modified friction stir clinching of AA2024-AA6061 aluminum alloys: Effects of materials positioning. *J. Mater. Res. Technol.* **2020**, *9*, 6037–6047. [\[CrossRef\]](#)
32. Kumar, R.; Salah, A.N.; Kant, N.; Singh, P.; Hashmi, A.W.; Malla, C. Effect of FSW process parameters on mechanical properties and microstructure of dissimilar welded joints of AA2024 and AA6082. *Mater. Today Proc.* **2022**, *50*, 1435–1441. [\[CrossRef\]](#)
33. Mohapatra, D.K.; Mohanty, P.P. Parametric Studies of Dissimilar Friction Stir Welded AA2024/AA6082 Aluminium Alloys. In *Recent Advances in Mechanical Engineering*; Springer: Berlin/Heidelberg, Germany, 2023; pp. 191–200.
34. Nalla Mohamed, M.; Sivaprasad, R. An Efficient Energy Absorber Based on Welded Fold Tubes for Automotive Applications. *Trends Mech. Biomed. Des. Sel. Proc. ICMEchD* **2021**, *2019*, 251–259. [\[CrossRef\]](#) [\[PubMed\]](#)
35. Elyasi, M.; Modanloo, V. Assessment of Energy Absorption and Crushing Performance of Perforated Thin-Walled AA6061-O Tubes with Irregular Holes Under Axial Compression Loading. *Arab. J. Sci. Eng.* **2024**, *49*, 1–12. [\[CrossRef\]](#)
36. Tiwan, H.; Iman, M.N.; Kusmono, K. Effect of Pin Geometry and Tool Rotational Speed on Microstructure and Mechanical Properties of Friction Stir Spot Welded Joints in AA2024-O Aluminum Alloy. *Int. J. Eng.* **2021**, *34*, 1949–1960. [\[CrossRef\]](#)
37. Forouzes, M.; Kazeminezhad, M. On the solution treatment of severely deformed AA2024-O and subsequent natural aging. *J. Mater. Res. Technol.* **2022**, *20*, 1558–1569. [\[CrossRef\]](#)
38. İpekoğlu, G.; Erim, S.; Kural, B.G.; Çam, G. Investigation into the effect of temper condition on friction stir weldability of AA6061 Al-alloy plates. *Kovove Mater.* **2013**, *51*, 155–163. [\[CrossRef\]](#)
39. El-Deeb, M.S.S.; Khorshed, L.A.; Abdallah, S.A.; Gaafer, A.M.; Mahmoud, T.S. Effect of friction stir welding process parameters and post-weld heat treatment on the corrosion behaviour of AA6061-O aluminum alloys. *Egypt. J. Chem.* **2019**, *62*, 1367–1375. [\[CrossRef\]](#)
40. Karmanov, V.V.; Kameneva, A.L. Dependence of the microstructure and microhardness of the AA2024-O alloy on the thermal and mechanical action on the weld during friction stir welding. *IOP Conf. Series Mater. Sci. Eng.* **2018**, *447*, 012058. [\[CrossRef\]](#)
41. Wang, P.; Gebert, A.; Yan, L.; Li, H.; Lao, C.; Chen, Z.; Kosiba, K.; Kuehn, U.; Scudino, S. Corrosion of Al-3.5Cu-1.5 Mg-1Si alloy prepared by selective laser melting and heat treatment. *Intermetallics* **2020**, *124*, 106871. [\[CrossRef\]](#)
42. López-Fernández, J.; Centeno, G.; Vallengano, C. Wrinkling in shrink flanging by single point incremental forming. *Int. J. Mech. Sci.* **2023**, *240*, 107930. [\[CrossRef\]](#)

43. Moradi, M.M.; Aval, H.J.; Jamaati, R. Effect of pre and post welding heat treatment in SiC-fortified dissimilar AA6061-AA2024 FSW butt joint. *J. Manuf. Process.* **2017**, *30*, 97–105. [\[CrossRef\]](#)
44. Maji, P.; Nath, R.K.; Karmakar, R.; Paul, P.; Meitei, R.B.; Ghosh, S.K. Effect of post processing heat treatment on friction stir welded/processed aluminum based alloys and composites. *CIRP J. Manuf. Sci. Technol.* **2021**, *35*, 96–105. [\[CrossRef\]](#)
45. Laska, A.; Szkodo, M.; Koszelow, D.; Cavaliere, P. Effect of Processing parameters on strength and corrosion resistance of friction stir-welded AA6082. *Metals* **2022**, *12*, 192. [\[CrossRef\]](#)
46. Machado, C.d.S.C.; Donatus, U.; Milagre, M.X.; Araujo, J.V.d.S.; de Viveiros, B.V.G.; Klumpp, R.E.; Pereira, V.F.; Costa, I. How microstructure affects localized corrosion resistance of stir zone of the AA2198-T8 alloy after friction stir welding. *Mater. Charact.* **2021**, *174*, 111025. [\[CrossRef\]](#)
47. Jandaghi, M.R.; Pouraliakbar, H.; Saboori, A.; Hong, S.I.; Pavese, M. Comparative insight into the interfacial phase evolutions during solution treatment of dissimilar friction stir welded AA2198-AA7475 and AA2198-AA6013 aluminum sheets. *Materials* **2021**, *14*, 1290. [\[CrossRef\]](#) [\[PubMed\]](#)
48. Sasikumar, A.; Gopi, S.; Mohan, D.G. Effect of welding speed on mechanical properties and corrosion resistance rates of filler induced friction stir welded AA6082 and AA5052 joints. *Mater. Res. Express* **2021**, *8*, 066531. [\[CrossRef\]](#)
49. Arbegast, W.J. A flow-partitioned deformation zone model for defect formation during friction stir welding. *Scr. Mater.* **2008**, *58*, 372–376. [\[CrossRef\]](#)
50. Gencer, G.M.; Oztoprak, N.; Serindag, H.T. Comparative experimental study on the modification of microstructural and mechanical properties of friction stir welded and gas metal arc welded EN AW-6061 O aluminum alloys by post-weld heat treatment. *Mater. Werkst.* **2018**, *49*, 1059–1067. [\[CrossRef\]](#)
51. Takhakh, A.M. Formability of Friction Stir Welded and Processed AA 2024–O Aluminum Alloy Sheets. *Adv. Nat. Appl. Sci.* **2016**, *11*, 10.
52. Chanakyan, C.; Sivasankar, S.; Alagarsamy, S.; Kumar, S.D.; Sakthivelu, S.; Meignanamoorthy, M.; Ravichandran, M. Parametric optimization for friction stir welding with AA2024 and AA6061 aluminium alloys by ANOVA and GRG. *Mater. Today Proc.* **2020**, *27*, 707–711. [\[CrossRef\]](#)
53. Sadeesh, P.; Kannan, M.V.; Rajkumar, V.; Avinash, P.; Arivazhagan, N.; Ramkumar, K.D.; Narayanan, S. Studies on Friction Stir Welding of AA 2024 and AA 6061 Dissimilar Metals. *Procedia Eng.* **2014**, *75*, 145–149. [\[CrossRef\]](#)
54. Jagathesh, K.; Jenarthanan, M.; Babu, P.D.; Chanakyan, C. Analysis of factors influencing tensile strength in dissimilar welds of AA2024 and AA6061 produced by Friction Stir Welding (FSW). *Aust. J. Mech. Eng.* **2015**, *15*, 19–26. [\[CrossRef\]](#)
55. Devaraju, A.; Shalem, M.J.; Manichandra, B. Effect of rotation speed on tensile properties & microhardness of dissimilar Al alloys 6061-T6 to 2024 -T6 welded via solid state joining technique. *Mater. Today Proc.* **2019**, *18*, 3286–3290. [\[CrossRef\]](#)
56. Devaraj, J.; Ziout, A.; Abu Qudeiri, J.E. Dissimilar non-ferrous metal welding: An insight on experimental and numerical analysis. *Metals* **2021**, *11*, 1486. [\[CrossRef\]](#)
57. ASTM E8/E8M-22; Standard Test Methods for Tension Testing of Metallic Materials. ASTM: Conshohocken, PA, USA, 2022; pp. 1–12. Available online: https://www.astm.org/e0008_e0008m-22.html (accessed on 15 May 2024).
58. ASTM E3-11; Standard Guide for Preparation of Metallographic Specimens. American Society for Testing and Materials United States of America: Conshohocken, PA, USA, 2017.
59. ASTM. Standard test method for microindentation hardness of materials. *ASTM Int.* **2017**, *384*, 1–40.
60. ASTM G69-20; Standard Test Method for Measurement of Corrosion Potentials of Aluminum Alloys. ASTM: Conshohocken, PA, USA, 2020; pp. 1–3. Available online: <https://www.astm.org/g0069-20.html> (accessed on 15 May 2024).
61. ASTM G5-14; Standard Reference Test Method for Making Potentiodynamic Anodic Polarization Measurements. ASTM: Conshohocken, PA, USA, 2014.
62. Oztoprak, N.; Yeni, C.E.; Kiral, B.G. Effects of post-weld heat treatment on the microstructural evolution and mechanical properties of dissimilar friction stir welded AA6061+SiCp/AA6061-O joint. *Lat. Am. J. Solids Struct.* **2018**, *15*, e49. [\[CrossRef\]](#)
63. Arsyad, H.; Arma, L.H. The Roughness Characteristic of AA6061-F, AA6061-O and AA6061-T6 after Machining Process. *IOP Conf. Ser. Mater. Sci. Eng.* **2020**, *875*, 012057. [\[CrossRef\]](#)
64. Wang, P.; Lei, Y.; Qi, J.F.; Yu, S.J.; Setchi, R.; Wu, M.W.; Eckert, J.; Li, H.C.; Scudino, S. Wear behavior of a heat-treatable al-3.5 cu-1.5 mg-1Si alloy manufactured by selective laser melting. *Materials* **2021**, *14*, 7048. [\[CrossRef\]](#)
65. Ilman, M.N. Microstructure and mechanical performance of dissimilar friction stir spot welded AA2024-O/AA6061-T6 sheets: Effects of tool rotation speed and pin geometry. *Int. J. Light. Mater. Manuf.* **2023**, *6*, 1–14. [\[CrossRef\]](#)
66. Dialami, N.; Cervera, M.; Chiumenti, M. Defect formation and material flow in Friction Stir Welding. *Eur. J. Mech.—A/Solids* **2020**, *80*, 103912. [\[CrossRef\]](#)
67. Kumar, K.; Kailas, S.V. The role of friction stir welding tool on material flow and weld formation. *Mater. Sci. Eng. A* **2008**, *485*, 367–374. [\[CrossRef\]](#)
68. Rajendran, C.; Abdulriyazdeen, A.; Abishek, S.; Aatheeshwaran, A.; Akash, A. Prediction of relationship between angular velocity to the pitch line velocity (ω/v) on tensile strength of friction stir welded AA2014-T6 aluminium alloy joints: Angular velocity to pitch line velocity ratio on FSW joints. *Forces Mech.* **2021**, *4*, 100036.
69. Asadi, P.; Aliha, M.; Akbari, M.; Imani, D.; Berto, F. Multivariate optimization of mechanical and microstructural properties of welded joints by FSW method. *Eng. Fail. Anal.* **2022**, *140*, 106528. [\[CrossRef\]](#)

70. Sun, Y.; Liu, W.; Li, Y.; Gong, W.; Ju, C. The Influence of Tool Shape on Plastic Metal Flow, Microstructure and Properties of Friction Stir Welded 2024 Aluminum Alloy Joints. *Metals* **2022**, *12*, 408. [[CrossRef](#)]
71. Cavaliere, P.; De Santis, A.; Panella, F.; Squillace, A. Effect of welding parameters on mechanical and microstructural properties of dissimilar AA6082–AA2024 joints produced by friction stir welding. *Mater. Des.* **2009**, *30*, 609–616. [[CrossRef](#)]
72. Nam, N.; Dai, L.; Mathesh, M.; Bian, M.; Thu, V. Role of friction stir welding—Traveling speed in enhancing the corrosion resistance of aluminum alloy. *Mater. Chem. Phys.* **2016**, *173*, 7–11. [[CrossRef](#)]
73. Kang, J.; Fu, R.-D.; Luan, G.-H.; Dong, C.-L.; He, M. In-situ investigation on the pitting corrosion behavior of friction stir welded joint of AA2024-T3 aluminium alloy. *Corros. Sci.* **2010**, *52*, 620–626. [[CrossRef](#)]
74. Nisancioglu, K.; Holtan, H. Measurement of the critical pitting potential of aluminium. *Corros. Sci.* **1978**, *18*, 835–849. [[CrossRef](#)]
75. Vikas, K.S.R.; Ramana, V.V.; Mohammed, R.; Reddy, G.M.; Rao, K. Influence of post weld heat treatment on microstructure and pitting corrosion behavior of dissimilar aluminium alloy friction stir welds. *Mater. Today Proc.* **2019**, *15*, 109–118. [[CrossRef](#)]

Disclaimer/Publisher’s Note: The statements, opinions and data contained in all publications are solely those of the individual author(s) and contributor(s) and not of MDPI and/or the editor(s). MDPI and/or the editor(s) disclaim responsibility for any injury to people or property resulting from any ideas, methods, instructions or products referred to in the content.